General Disclaimer

One or more of the Following Statements may affect this Document

- This document has been reproduced from the best copy furnished by the organizational source. It is being released in the interest of making available as much information as possible.

- This document may contain data, which exceeds the sheet parameters. It was furnished in this condition by the organizational source and is the best copy available.

- This document may contain tone-on-tone or color graphs, charts and/or pictures, which have been reproduced in black and white.

- This document is paginated as submitted by the original source.

- Portions of this document are not fully legible due to the historical nature of some of the material. However, it is the best reproduction available from the original submission.

Produced by the NASA Center for Aerospace Information (CASI)

NASA TECHNICAL MEMORANDUM

NASA TM-73821

NASA TM-73821

(NASA-TM-73821) SYNTHESIS OF BLADE FLUTTER VIBRATORY PATTERNS USING STATIONARY TRANSDUCERS (NASA) 26 p HC A03/MF A01 CSCL 01A

N78-17001

Unclas
G3/02 04485

SYNTHESIS OF BLADE FLUTTER VIBRATORY PATTERNS USING STATIONARY TRANSDUCERS

by A. Kurkov and J. Dicus
Lewis Research Center
Cleveland, Ohio 44135

TECHNICAL PAPER to be presented at the
Gas Turbine Conference sponsored by the
American Society of Mechanical Engineers
London, England, April 9-13, 1978

FEB 1978
RECEIVED
NASA STI FACILITY

SYNTHESIS OF BLADE FLUTTER VIBRATORY PATTERNS USING STATIONARY TRANSDUCERS

by A. Kurkov and J. Dicus

National Aeronautics and Space Administration

Lewis Research Center

Cleveland, Ohio 44135

ABSTRACT

Flutter frequency was determined and rotor vibratory amplitude and phase distributions during flutter were reconstructed from stationary aerodynamic type measurements. A previously reported optical method for measuring blade-tip displacement during flutter was extended by means of digital analysis. Displacement amplitudes and phase angles were determined based on this method. For selected blades, spectral results were also obtained from strain gage measurements. The results from these three types of measurement were compared and critically evaluated.

E-9410

NOMENCLATURE

A	amplitude in rotating frame of reference
A_i	i^{th} amplitude in stationary frame
E	engine order
F	Fourier transform
f	frequency
j	imaginary unit
N	number of points

STAR Category 39

N_i	i^{th} nodal diameter
N_t	total number of nodal diameters
n	number of blades
t	time
α	angular separation between two sensors
ϵ	defined in Appendix
ϕ	phase angle in rotating frame
$\Delta\phi$	phase lag due to rotation
ϕ_i	phase corresponding to i^{th} amplitude
φ	angular coordinate in rotating frame
$\Delta\varphi$	angular separation between two blades
ω	circular frequency
ω_r	rotational frequency

INTRODUCTION

Most commonly, turbomachinery flutter instrumentation consists of blade mounted strain gages. Recently, however, two alternative schemes [1][1] that rely on optical measurement techniques were successfully implemented in a full scale engine research facility. One scheme produced the display of the stroboscopic image (SI) of the tip of the blade during flutter. The other scheme, termed Photoelectric Scanning method (PES), resulted in the screen display of the extremes of the blade-tip displacements for each blade. This second technique was found to be particularly useful for flutter monitoring. Quantitative measurements, however, were limited to the determination of vibratory displacement amplitudes based on photographs of PES screen display.

---

[1]Numbers in brackets designated References at the end of the paper.

In this paper the use of stationary sensors such as in reference [1] is explored further. Particular attention is given to quantitative analyses which until now were limited in extent. This has been achieved mainly through the use of digital analysis techniques. It is anticipated that with further development of analysis and instrumentation techniques, the reliance on strain gages and the associated signal transmission hardware could be greatly reduced.

It is shown in the first part of the paper that flutter can be detected from the data recorded by the air-stream (i.e. aerodynamic) instrumentation. A method is presented which allows construction of the rotor vibratory pattern from these measurements. It relies on digital spectral analysis procedures incorporating Fast Fourier Fransform (FFT) algorithm. A method is also presented which allows precise determination of flutter frequency based on measurements provided by two aerodynamic transducers.

The second part of the paper deals with PES data. In the present case, however, the displacement are obtained by means of digital analysis of the blade sensor and reference sensor signals. These signals were recorded on a magnetic tape during flutter testing. Once the relative displacements are obtained for a number of rotor revolutions, spectral analysis techniques are applied to obtain vibratory amplitude and phase angles. In this case the spectral analysis is also based on the FFT procedure.

Optical and aerodynamic data were available for the same test point so that detailed comparison of the spectral results from both

methods was possible. The results exhibited similar specific features associated with the fact that these sensors are stationary and not blade mounted. Since a number of blades were also strain gaged, both stationary and blade mounted vibratory measurements were available for these blades enabling comparison of results from these two types of measurements.

It should be noted that another optical method for measuring of blade displacements during flutter has been recently implemented [2]. Some additional information related to the use of stationary sensors is available in reference [3]. Both, flutter and resonant blade vibrations are included.

The data presented in the paper were obtained during the first fan-rotor flutter test of a preproduction turbofan engine in an altitude test facility. Flutter was classified as "stall flutter." It occurred in the neighborhood of 70 percent of the design speed at high incidence and under elevated inlet pressure and temperature conditions. Stress levels during flutter were about 3.5 kN/cm^2 (5 ksi). The vibratory mode was identified to be predominantly torsional.

AERODYNAMIC FLUTTER-INSTRUMENTATION

The first fan-rotor case was instrumented with a number of high-response static pressure transducers. The transducers were very nearly flush-mounted. Six transducers were installed in the fan case approximately in the direction of the rotor blade chord at the tip span. The first transducer was aligned with the blade leading edge and the sixth with the blade trailing edge. Several transducers were also in-

stalled in the fan case corresponding to rotor blade midchord position and spaced circumferentially one blade pitch apart.

For a limited number of test points, the first-rotor discharge (i.e. rotor wake) was instrumented with a high-response probe in the form of a miniature cantilever beam [4]. Its response was proportional to the lift force acting on the cantilevered beam. The measurements with this probe were obtained at about 90 percent of the blade span. The responses of the cantilevered beam and the static pressure transducers were sufficiently high to capture the blade passing frequency, as well as its significant harmonics. The data from these measurements were recorded on a multichannel FM magnetic tape recorder at 304.8 cm/s (120 in/s).

SPECTRAL ANALYSIS OF AERODYNAMIC DATA

The spectral analysis of aerodynamic data was performed on a digital spectral analyzer which could be programmed to perform special functions in addition to the standard functions. A summary of the parameters used in the spectral analysis and the description of the special procedures incorporated in the analysis are given in the Appendix.

Figure 1 illustrates the power spectrum of the wake-probe transducer signal during flutter, and Fig. 2 in the absence of flutter. The engine corrected operating conditions corresponding to these figures were the same; however, Fig. 1 corresponded to a higher engine inlet pressure. Frequencies in these figures were normalized using shaft rotational frequency, that is, they were expressed in engine orders. To facilitate interpretation of the results, the frequency corresponding

to each significant peak was written just above that peak. Normalized flutter frequency based on strain gage measurements is also included in Fig. 1.

The amplitudes in Figs. 1 and 2 are normalized with respect to the highest peaks. This is found to be convenient for the purpose of comparison of spectral results based on measurements obtained with different types of transducers.

Inspection of these figures reveals that discrete nonintegral order frequencies are characteristic of flutter and that they differ from flutter frequency by an intregral number of engine orders, within the available resolution accuracy. Each nonintegral order frequency corresponds to a different travelling wave. This follows from the fact that a N_i-nodal diameter wave motion described in a frame of reference fixed with respect to the rotor by

$$A_i \cos(\omega t \mp \varphi N_i + \phi_i)$$

transforms into

$$A_i \cos[(\omega \pm \omega_r N_i)t + \phi_i]$$

in a stationary reference frame. The upper and lower signs in these expressions correspond to forward and backward moving waves, respectively.

Flutter could also be detected from the static pressure transducer signals. For example, Fig. 3 presents a power spectral plot that corresponds to a midchord static pressure transducer. Comparing Figs. 1 and 3 it is seen that there exists a reasonable agreement among the relative magnitudes of flutter peaks. Spectral plots corresponding

to other midchord transducers are qualitatively quite similar. At the leading edge, however, sharp attenuation of high frequency nodal diameter waves is observed, Fig. 4. Although the trailing edge static pressure transducer was inoperative for this test point, evidence from other test points during which this transducer was operational indicates a similar attenuation of the high-frequency nodal waves. Since these nodal waves were well reproduced in Fig. 1, which is based on measurements in the rotor wakes at 90 percent of the blade span, this suggests that the attenuation phenomenon is due to the specific features of the flow in the immediate vicinity of the casing wall in the blade trailing-edge and possibly leading-edge regions. This observation has obvious practical significance in cases where it is desired to use static pressure transducers for investigation of flutter.

AMPLITUDE AND PHASE ANGLES

In this section the rotor vibratory pattern including both, amplitude and phase angles is constructed from a pressure transducer signal. A different test point is selected for this purpose, mainly because detailed optical sensor data are also available for this point. For the present purpose, it is essential to be able to determine rotor orientation at time $t = 0$, corresponding to the start of the data sampling. The start of sampling was, therefore, triggered using once-per-revolution signal pulse.

The linear spectral plot (i.e., the magnitude of the Fourier transform) corresponding to a midchord static pressure transducer is presented in Fig. 5. While in Figs. 1 and 3 one could identify a pre-

dominantly three nodal diameter forward travelling wave pattern, in Fig. 5 no single wave pattern is dominant. In addition to the nodal-wave amplitudes (A_i) represented in Fig. 5, one also needs the corresponding phase angles (ϕ_i). Their determination is discussed in the Appendix. Basically, it involves an interpolation process which becomes necessary because of an inherent feature of results obtained with the FFT procedure [5]. Once A_i's and ϕ_i's are determined, transformation into a rotating frame of reference and superposition is accomplished using the following equation,

$$\sum_{i=1}^{N_t} A_i e^{j(\omega t - \varphi N_i + \phi_i)} = A(\varphi) e^{j(\omega t + \phi(\varphi))} \qquad (1)$$

where A and ϕ represent amplitude and phase in the rotating frame of reference, and $\varphi = 0$ denotes the rotor radius pointing to the transducer position at time $t = 0$. (The radius $\varphi = 0$, approximately corresponded to blade number 19.) The sign of N_i in the above equation is either positive or negative depending on whether the wave is forward or backward. Thus, referring to Fig. 5, at frequency $f = 11.45$, $N_i = 3$; and at $f = 5.45$, $N_i = -3$. All amplitudes corresponding to nonintegral frequencies marked in Fig. 5, with the exception of the amplitude at $f = 10.447$, were included in the summation. Consequently, N_t was 9 in equation (1).

The results of superposition are presented in Figs. 6 and 7. The amplitudes in these figures were normalized with respect to blade number one, and the phase angles were evaluated relative to blade number

one. Blade positions were identified with an accuracy of about one half of the blade pitch. Large amplitude and phase angle variations evident in Figs. 6 and 7 are typical of the "mistuned rotor" response [6]. These results will be compared later with the strain gage and optical displacement measurements.

DETERMINATION OF FREQUENCY

The results presented in the previous section could not have been derived without the knowledge of flutter frequency, because there would be no basis for selection of N_i corresponding to each nonintegral engine order peak. Flutter frequency may be obtained from the strain gage data, or it may be known within the accuracy of one engine order. However, frequency can also be determined precisely and without any previous knowledge if two aerodynamic sensors located at different circumferential positions around the rotor are available. It is necessary to determine the phase difference between the outputs of two transducers at only one nonintegral engine order frequency. This phase difference is then equated to $\alpha \cdot N_i$, where α is the angular separation between two transducers and N_i the desired nodal diameter number. Once one N_i is determined, the others can be determined by observing relative frequencies. Table 1 illustrates these phase relationships for two midchord transducers with $\alpha = 47.4^{o}$. Rather than calculating N_i in the last column, for illustrative purposes it is more convenient to use the known N_i's to calculate the phase angles. The agreement between these (column 3) and the phase angles obtained from direct measurement (column 2) is particularly satisfactory for backward travelling waves.

OPTICAL-SENSOR SIGNAL ANALYSIS

A brief description of the physical arrangement of different sensors employed in the PES method is included here in order to facilitate the explanation of the analysis procedure. The information related to the optical probe design is available in reference [1]. In this method, measurements are provided by four sensors. Two optical type sensors were used to detect blade tip positions, while two magnetic type sensors provided reference signals related to the shaft rotational frequency and the blade passing frequency. One of the optical sensors was positioned opposite the blade trailing edge position, and the other opposite the blade midchord. The choice for these positions, to some extent, was determined by the availability of an access port in the fan case. As the blade tips passed by each sensor, a series of pulses were generated and recorded on the magnetic tape. Also recorded on the magnetic tape were the pulse signals corresponding to the rotational frequency and the blade passing frequency. The latter were generated by a shaft mounted gear having the same number of teeth as the number of blades.

The four channels of data were recorded on a multi-channel direct-record type tape recorder at 304.8 cm/s (120 in/s). Subsequently, these data were recorded on an FM tape recorder at 304.8 cm/s (120 in/s) playing back the original tape at 7.62 cm/s (30 in/s). The latter FM tape was then digitized at 9.525 cm/s (3.75 in/s) at the rate of 10 kHz per channel. In terms of real time, the resulting digitizing rate was 1.28 MHz. The remaining data processing was performed on a digital computer. It involved computation of relative time of occurrence of

different pulses. For example, in order to compute trailing edge displacements, it was necessary to calculate the time difference between the occurrences of trailing edge pulse and the closest reference blade-passing-frequency pulse, for each blade and every revolution. The deviations about the average of these time differences are proportional to displacements during flutter. Special care had to be taken to avoid occasional spurious signals which were probably due to air particle-contamination. The particles could either emit or reflect the light.

The results of this procedure are illustrated in Fig. 8 where each unit corresponds to a trailing edge displacement of about 0.27 mm (0.0106 in). The data frame for this figure corresponds to 27 rotor revolutions. (Note that some of the points overlap in Fig. 8.) It should be noted that analogous to trailing-edge displacements, the midchord, and the trailing edge relative to midchord displacements can be evaluated. These displacements, however, are not as large, so that in order to achieve a reasonable accuracy, more points per blade passage and, therefore, a higher digitizing rate than the one used for Fig. 8 is necessary.

SPECTRAL ANALYSIS OF BLADE DISPLACEMENTS

Spectral analysis of the displacements represented in Fig. 8 can be performed in two ways. One is to include displacement from all blades in the order they were sampled (sampling rate 38E), and the other is to analyze displacements corresponding to each blade separately (sampling rate 1E). The overall spectrum, corresponding to the sampling rate of 38E, is given in Fig. 9. The units in this figure are

the same as in Fig. 8. Because of the nature of the sampling process, only flutter, or nonintegral engine order vibrations are detected. Therefore, for the purpose of comparison of results included in Figs. 5 and 9, only nonintegral order amplitudes in Fig. 5 are relevant. These amplitudes are seen to be in approximately the same relative proportions in the two figures.

An example of a spectrum plot for a single blade corresponding to the sampling rate of 1E is included in Fig. 10. As a direct consequence of the sampling theorem [5], the frequencies in this figure are aliased between zero and one half engine order. Frequency information in this figure is, therefore, more indeterminate than in Fig. 9, that is, it is only known by how much flutter frequency differs from a multiple of 1/2E, and not 1E frequency, as in Fig. 9. Precise determination of flutter frequency, as already discussed during the analysis of static-pressure-transducer data, requires two sensors. Only one trailing-edge sensor was available in the present investigation, so that this procedure could not be repeated for the optical data; however, based on spectral plots, one can expect similar consistency of results as in Table 1. In the absence of a system mode of vibrations, that is, when each blade vibrates at a frequency different from any other blade, the number of sensors should exceed two times the flutter frequency expressed in engine orders. For the system mode, there is an upper limit on the highest nodal diameter which can be detected with one sensor:

$$N_i < n/2 - f$$

where f is the flutter frequency in engine orders.

Referring to Fig. 9, an additional interpretation of spectral peaks in this figure is possible based on the orthogonality property of nodal waves. Squaring and integrating real and imaginery parts in equation (1) between the limits of $-\Pi$ to Π, one obtains

$$\frac{1}{2\pi}\int_{-\Pi}^{\Pi} A^2 d\varphi = \sum_{i=1}^{N_t} A_i^2$$

which relates the amplitudes in Fig. 9 to the rotor-mean squared displacement amplitudes.

By performing spectral analysis separately for each blade, displacement amplitude and phase distributions around the rotor can be constructed. It should be noted, however, that in relating the phase angles from different blades, an account has to be taken of the fact that blades were not sampled simultaneously. Between any two blades there exists a phase lag due to the rotation. It is given by

$$\Delta\phi = \Delta\varphi \cdot f$$

where $\Delta\varphi$ is the angular separation between two blades, and f is flutter frequency expressed in engine orders. The amplitude and phase angle distributions are presented in the next section where they are also compared with corresponding results from pressure and strain-gage measurements.

DISCUSSION OF RESULTS

The normalized amplitudes corresponding to pressure, displacement, and stress measurements are given in Fig. 11, and the relative phase angles corresponding to these measurements in Fig. 12. The

stress data in these figures were derived from two types of strain gages: the ASTE gage, located above the shroud and close to the trailing edge; and the TIP gage, located close to the blade tip and about one third of a chord length behind the leading edge. The strain gage located above the shroud at the maximum thickness point, and the gages below the shroud did not register any appreciable stresses.

The stress and displacement measurements are more directly related to the blade motion than the pressure measurement. The results based on these two methods can, therefore, be used to evaluate the accuracy of results derived from pressure measurements. It can be observed from Figs. 11 and 12 that amplitude and phase distributions derived from pressure measurements are qualitatively correct despite a lack of precise quantitative agreement. However, even approximate knowledge regarding vibratory amplitude and phase distributions can be valuable. Such information cannot be easily obtained from strain gage measurements because of their usually limited coverage.

The agreement between stress and displacement amplitudes in Fig. 11 is very good except for blades 25 and 30. Another unusual feature associated with blade 25 is the significant difference between normalized ASTE and TIP stresses. Examination of Fig. 12 indicates that differences between stress phase-angles and displacement phase-angles are within 20^{o}, and that in particular, blades 25 and 30 are no exceptions. It is noted that even if stress amplitude were in error, one would not expect the stress phase-angles to be in error. Examination of the change in resistance of these strain gages subsequent to the

test run, however, indicates that according to the established practice the change was insufficient to bring their accuracy into question [7]. Another cause for erroneous indication which cannot be ruled out is the supersensitivity phenomenon [8]. Substantiation of this cause, however, would require further investigation.

It appears, therefore, that positive identification of the cause of the above inconsistencies cannot be made at this point. However, the preceeding discussion does illustrate that in addition to providing displacements, the PES method can be used in conjunction with stress measurements to provide some degree of redundancy and, therefore, increase the confidence in measurements.

CONCLUSIONS

1. Flutter can be detected from high-response aerodynamic data records.

2. It is possible to obtain qualitatively correct distribution of vibratory amplitude and phase around the rotor from the data recorded by case-mounted static pressure transducers.

3. Precise determination of flutter frequency can be made using two stationary transducers.

4. Spectral displacement-amplitudes and phase angles during flutter can be obtained from the optical blade-tip position measurements.

APPENDIX

The spectral results presented in the main body of the paper were obtained based on specifications in Table 2.

The factor of 16 in columns 3 and 4 is present because the tape speed on the play-back was reduced 16 times. The engine order frequency was determined independently for each data frame by numerically detecting the blade passing frequency and then dividing it by the number of blades. Blade passing frequency was a predominant signal and it could be clearly detected despite the fact that it was beyond the filter cut-off frequency. The filter roll-off rate was 48 db per octave.

Spectral analysis corresponding to Figs. 8 and 9 was performed on a large computer using an algorithm developed by Singleton [9]. A convenient feature of this program is that the number of points in a data sample does not have to be a power of two but it can be arbitrary. The program is included in the IMSL (International Mathematical and Statistical Libraries, Inc.) library.

The remainder of the Appendix is concerned with the determination of phase angles relative to the start of a data sample.

If the Fourier transform is applied to a digital data sample that contains a nonintegral number of cycles at a particular frequency, the results will be not one but several peaks clustered around that frequency. It is usually sufficiently accurate to determine frequency based on the highest peaks. However, the phase angle shifts by approximately 180^{o} between peaks on each side of the true frequency. This can be seen by applying a sinusoidal input to the Fourier transform [5]. For a data sample of N points the result is

$$\frac{1}{N} F(j\omega) = \frac{1}{N} \frac{\sin \epsilon \Pi}{\sin(\epsilon \Pi/N)} e^{j\epsilon \Pi(N-1)/N} \qquad (2)$$

where $\epsilon = (\omega_0 - \omega)/(2\Pi/NT)$, ω_0 is the frequency of the sinusoidal input and T the sampling interval. When $\omega = \omega_0$, the magnitude of the normalized Fourier transform $(1/N)F(j\omega)$ is one. However, if the highest peak occurs at ω_1, $\omega_1 < \omega_0$, and there is also a significant contribution at $\omega = \omega_2$, $\omega_2 > \omega_0$,

$$\frac{1}{N} \frac{\sin \epsilon_1 \Pi}{\sin(\epsilon_1 \Pi/N)} \sim \frac{A_1}{\sqrt{A_1^2 + A_2^2}}$$

where A_1 and A_2 are amplitudes corresponding to ω_1 and ω_2 respectively. Fraction ϵ_1, can therefore be estimated from this expression either numerically or graphically by plotting the left hand side. Once ϵ_1 is determined it follows from equation (2) that the phase angle at $\omega = \omega_0$ is equal to the phase angle at $\omega = \omega_1$ minus $\epsilon_1 \Pi(N - 1)/N$.

REFERENCES

1. Nieberding, W. C. and Pollack, J. L., "Optical Detection of Blade Flutter," ASME Paper No. 77-GT-66, Mar. 1977.
2. Stargardter, H., "Optical Determination of Rotating Fan Blade Deflections," ASME Paper No. 76-GT-48, Mar. 1976.
3. Zablotskii, I. E., et. al., "Contactless Measuring of Vibrations in the Rotor Blades of Turbines," Lopatochnyye Mashiny i Struynye Apparaty, No. 6, 1972, pp. 106-121; also: Technical Translation, Foreign Technology Division, Wright Patterson Air Force Base, Ohio FTD-HT-23-673-74, 1974.
4. Krause, L. N. and Fralick, G. C., "Miniature Drag-Force Anemometer," NASA TM X-3507, 1977.
5. Stearns, S. D., Digital Signal Analysis, Hayden, Rochelle Park, N. J., 1975.
6. El-Bayoumy, L. E. and Srinivasan, A. V., "Influence of Mistuning on Rotor-Blade Vibrations," AIAA Journal, Vol. 13, No. 4, Apr. 1975, pp. 460-464.
7. Holanda, R. and Krause, L., "Reliability Analysis of 45 Strain Gage Systems Mounted on the First Fan Stage of a YF-100 Engine," NASA TM-73724, 1977.
8. Drew, D. A., "High Temperature Strain Gage Techniques," Strain Gage Readings, Vol. VI, No. 4, 1963, pp. 11-25.
9. Singleton, R. C., "An Algorithm for Computing the Mixed Radix Fast Fourier Transform," IEEE Transactions in Audio and Electroacoustics, Vol. AU-17, No. 2, June 1969, pp. 93-103.

TABLE 1. - PHASE RELATIONSHIPS BETWEEN TWO TRANSDUCERS 47.4° APART

Frequency, E	Cross-power-spectrum phase, deg	Phase based on N_i, deg
3.45	122.0	123.0
4.45	173.6	170.5
5.45	-144.2	-142.1
6.43	- 93.7	- 94.7
8.44	- 3.3	0.0
11.46	150.0	142.1
12.45	-158.3	-170.5

TABLE 2. - PARAMETERS EMPLOYED IN SPECTRAL ANALYSES

Spectral results	Number of data points	Sampling frequency	Filter cut-off frequency	Number of data samples	Rotational frequency
Table 1	2048	819.2 · 16	200 · 16	16	127.31
Figs. 1, 3, and 4	4096	819.2 · 16	200 · 16	16	136.58
Fig. 2	4096	819.2 · 16	200 · 16	16	116.78
Fig. 5	8192	512 · 16	200 · 16	1	127.31
Fig. 8	1026	38E		1	127.31
Fig. 9	27	1E		1	127.31

Unless noted otherwise, all frequencies are in Hz.

REPRODUCIBILITY OF THE
ORIGINAL PAGE IS POOR

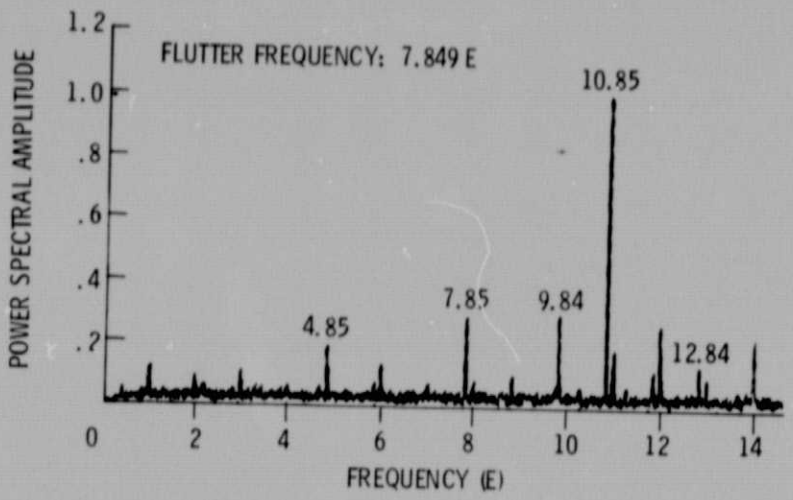

Fig. 1 Power spectrum of the wake-probe transducer signal during flutter.

E-9410

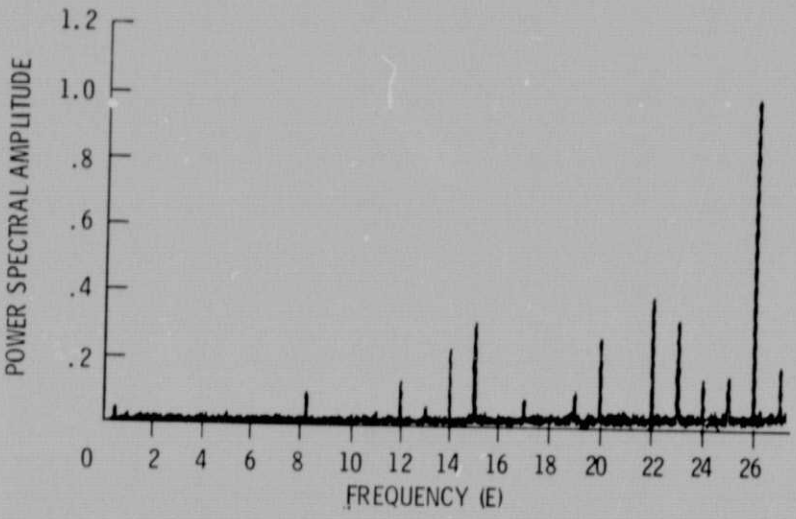

Fig. 2 Power spectrum of the wake-probe transducer signal; no flutter condition.

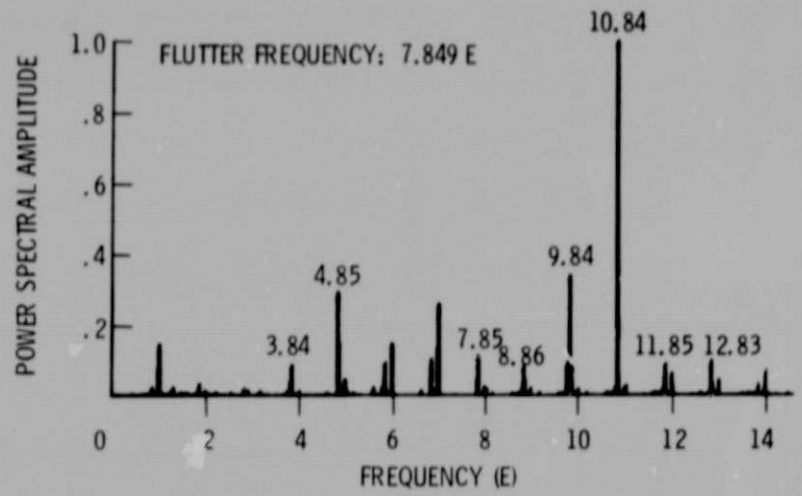

Fig. 3 Power spectrum of the midchord pressure transducer signal.

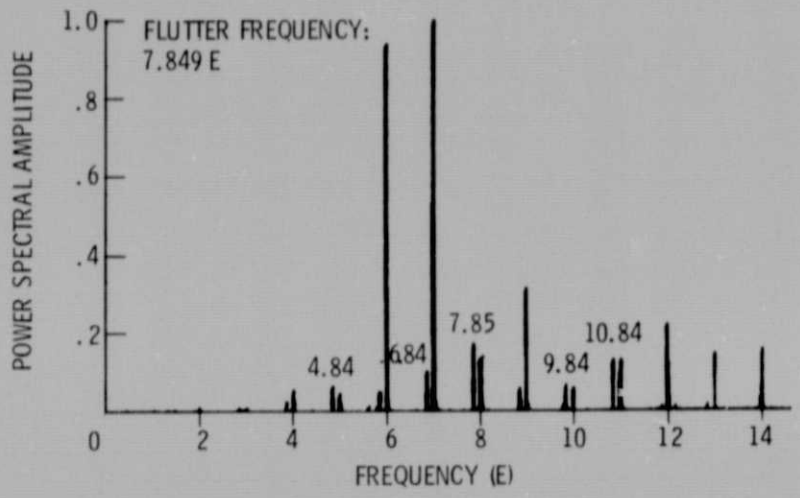

Fig. 4 Power spectrum of the leading-edge pressure transducer signal.

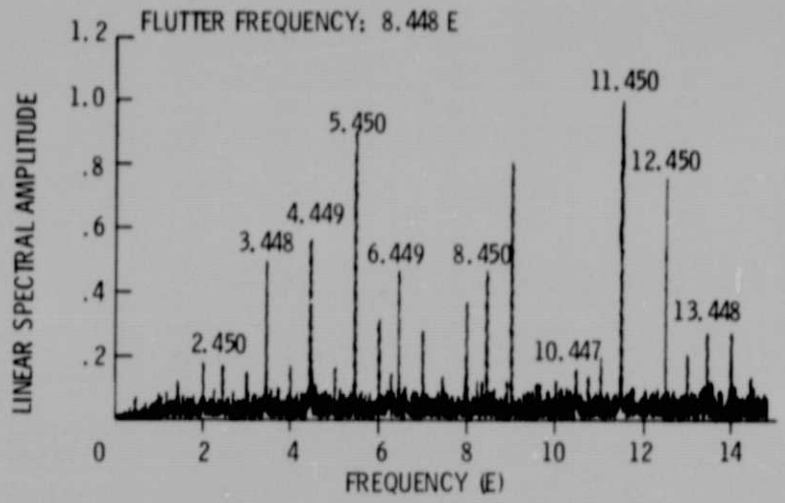

Fig. 5 Linear spectrum of the pressure transducer signal.

E-9410

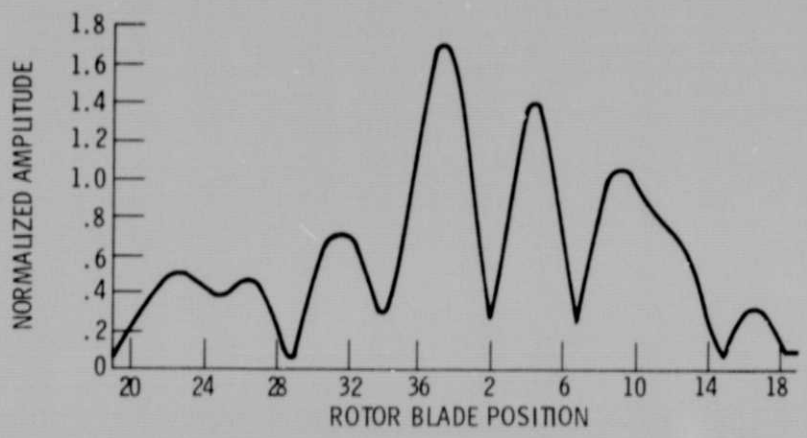

Fig. 6 Vibratory amplitude distribution from static pressure data.

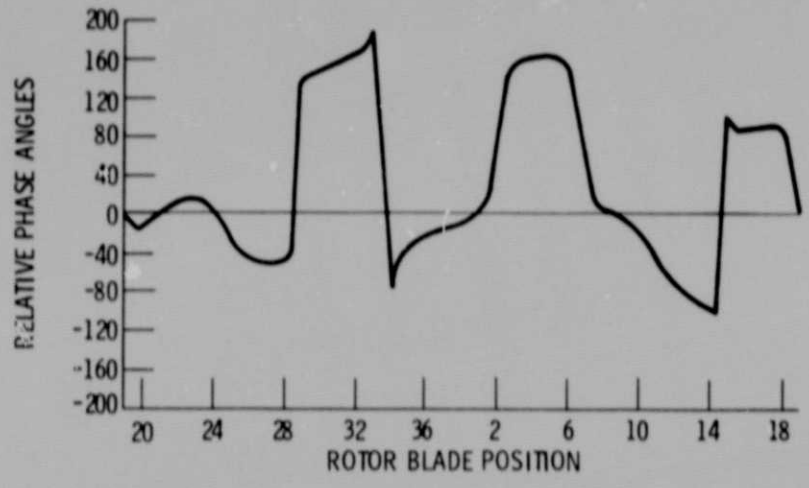

Fig. 7 Phase angle distribution from static pressure data.

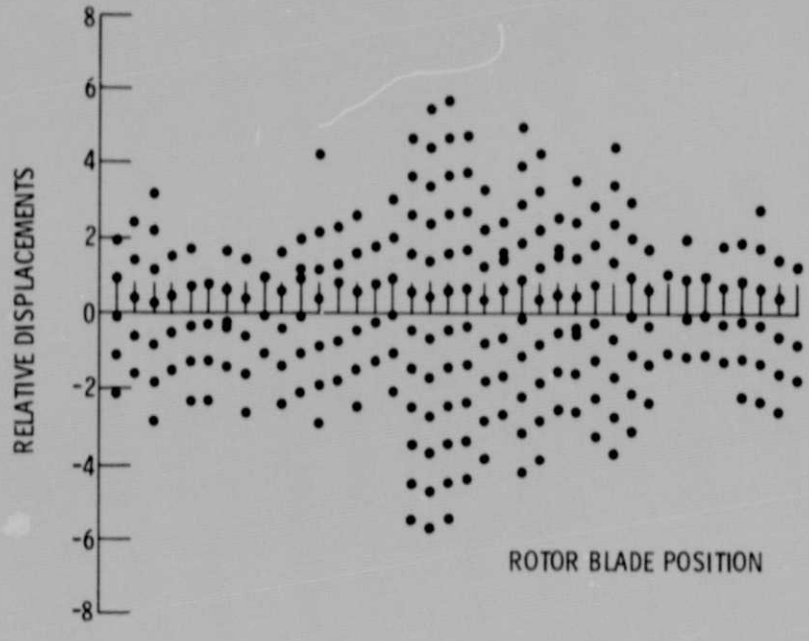

Fig. 8 Relative trailing edge displacements during flutter; 1 unit = 0.27 mm.

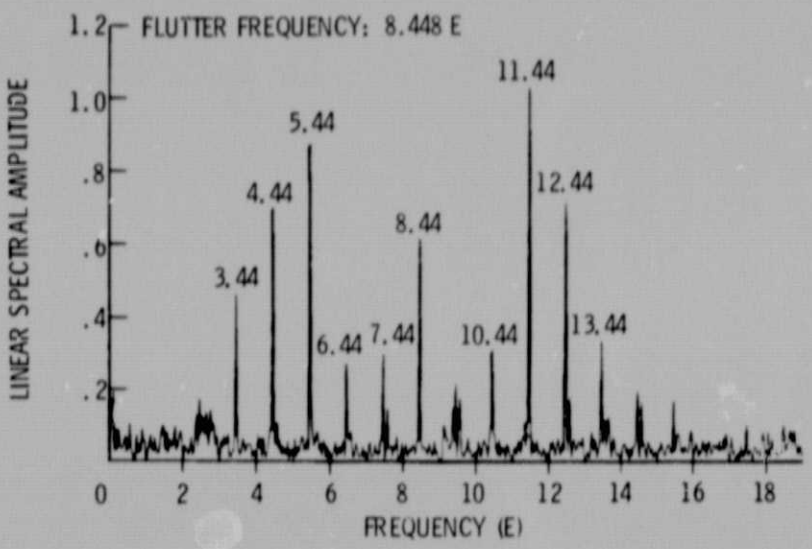

Fig. 9 Displacement-amplitude spectrum; 1 unit = 0.27 mm.

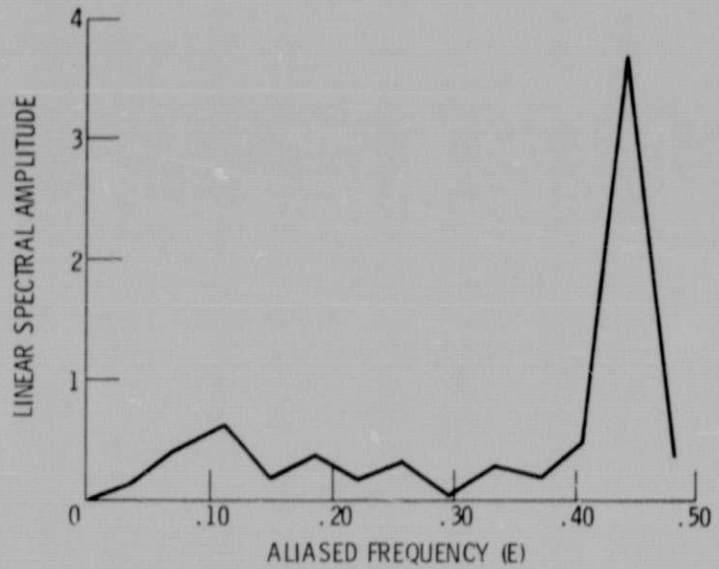

Fig. 10 Displacement-amplitude spectrum for blade no. 1; 1 unit = 0.27 mm.

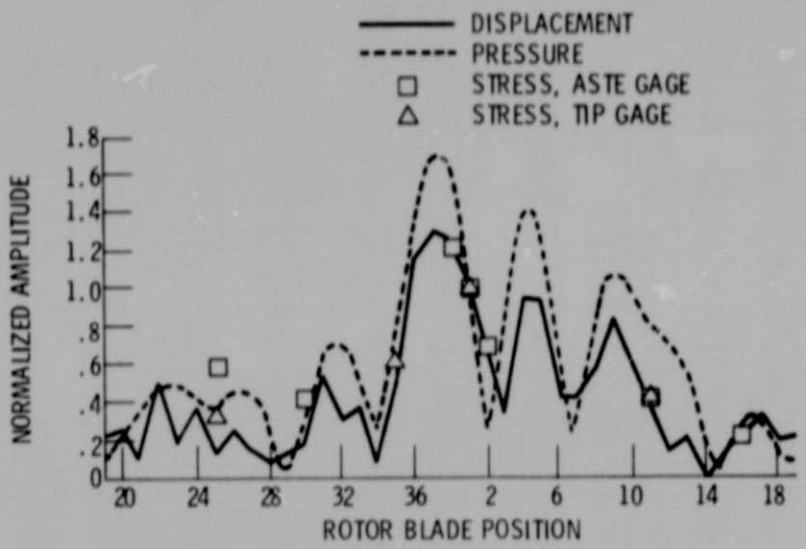

Fig. 11 Vibratory amplitude distribution at flutter frequency.

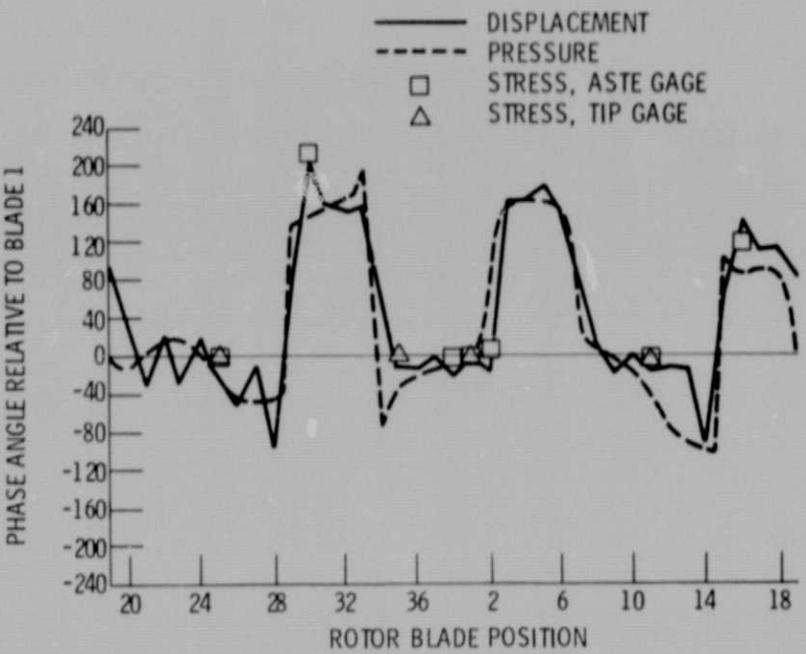

Fig. 12 Phase angle distribution at flutter frequency.

NASA-Lewis-Com'l